Modeling Sea Ice fracture at very high resolution with VP rheologies

Damien Ringeisen [1], Nils Hutter [1], Martin Losch [1], and L.Bruno Tremblay [2]

[1]Alfred-Wegener-Institut, Helmholtz-Zentrum für Polar und Meeresforschung (AWI), Bremerhaven, Germany
[2]Department of Atmospheric and Oceanic Sciences, McGill University, Montréal, Quebec, Canada

Correspondence: Damien Ringeisen (damien.ringeisen@awi.de)

Abstract. Recent high resolution pan-Arctic sea ice simulations show fracture patterns (Linear Kinematic Features - LKFs) that are typical of granular materials but with intersection (fracture) angles wider than those observed from high-resolution satellite images (with a modal value of $\theta = 20°$). In this article, We investigate the mechanism of formation and parameter dependencies of ice fracture in simple numerical bi-axial test on a $8\,\text{km}$ x $25\,\text{km}$ ice floe at an unprecedented resolution of $25\,\text{m}$ for two different yield curves: an elliptical (VP) and a Coulombic yield curve both with normal flow rule. In the standard VP model, the simulated angle of fracture is $\theta = 33.9°$, compared to $20°$ in observations. The dependence of the angle of fracture on the ice shear strength is also contrary to that of typical granular materials with larger angle of fracture for higher shear strength - think of a wet sand castle with steeper walls than a dry sand castle. In this model, the divergence along the fracture lines (or LKFs) is entirely dictated by the ice shear strength used in the model with high shear strength resulting in convergence along LKFs and low shear strength resulting in divergence along LKFs. This is again contrary to typical granular materials where divergence (or dilation) is linked with the orientation of contacts normals that oppose the flow with divergence present for larger shear resistance and convergence for lower shear resistance. Moreover, the angle of fracture depends on the confining pressure in the uni-axial test with more convergence as the confining pressure increases, again contrary to granular material that have an angle of fracture that is independent of the confining pressure. We note that all three behaviors of the VP model are linked with the use of an associative (normal) flow rule. In the Coulombic model, the angle of fracture is smaller ($\theta = 23.5°$), but the solution is unstable when the compressive stresses are too large because of the discontinuity between the straight limbs of the yield curve and the elliptical capping. Our results show that while the VP model gives angles of fracture that are visually correct, the bias in the magnitude of the angle of fracture and the physical dependencies of the angle of fracture on mechanical strength parameters and stress fields couple the sea ice mechanical strength parameters, the sea-ice drift, sea-ice deformation (strain-rate) field in an inconsistent way. We consider this evidence to move away from the elliptical yield curve and associative (normal) flow rule, a deformation law that is not applicable to pressure-sensitive and dilatant granular material such as sea ice.

1 Introduction

Sea ice is a granular material; i.e. a material that is composed of ice floes of different size and shape (Tremblay and Mysak, 1997; Overland et al., 1998). In most large-scale models used in the community, sea ice is treated as a continuum deforming plastically when the internal stresses reaches critical values in compression, shear and tension and deforming as a very

viscous (creeping) flow when the internal stresses are relatively small (e.g. Hibler (1979); Zhang and Hibler (1997); Hunke and Dukowicz (1997). Using modern numerical solvers, the highly non-linear sea-ice momentum equations can be solved to convergence to reproduce qualitatively observed patterns of sea ice deformation with reasonable computing time (Hutchings et al., 2005; Losch et al., 2010; Hutter et al., 2018a). These linear features where large shear and divergence are present are

5 called Linear Kinematic Features (LKFs) (Kwok, 2001). Lead opening along LKFs are the memory of such models, affecting the subsequent dynamics, mass balance, and the heat/salt exchanges between the ocean, ice and atmosphere. It is therefore important to investigate whether the mode of sea-ice fracture is represented accurately in continuum sea ice models.

The sea-ice momentum equations are difficult to solve numerically because of sharp spatial changes in material properties associated with discontinuities (e.g. along sea ice leads or ridges) and heterogeneity (different ice types) in the pack ice. Since

10 the birth of modern sea ice dynamics in the mid-seventies with the development of the Elastic-Plastic sea ice model based on data collected during the Arctic Ice Dynamics Joint Experiment (Coon et al., 1974, (AIDJEX)), several other approaches to modeling sea ice were developed. In these models, sea ice was treated as an incompressible fluid (Rothrock, 1975), a Viscous-Plastic (VP) material (Hibler, 1979), an Elastic-Viscous-Plastic (EVP) material (Hunke, 2001), a granular material (Tremblay and Mysak, 1997), an Elastic Anisotropic Plastic (EAP) medium (Wilchinsky and Feltham, 2006), an elastic-decohesive

15 medium (Schreyer et al., 2006), an Elasto-Brittle (EB) material (Rampal et al., 2016) and a Visco-Elastic-Brittle (MEB) material (Dansereau et al., 2016). The actual diversity in approaches to sea-ice modeling in the community however is much smaller; e.g. 30 out of 33 Global Climate Models use some form of the standard VP rheology Stroeve et al. (2014).

In spite of its success, the standard VP rheology is not undisputed. Coon et al. (2007) critically reviewed the assumptions behind current modeling practice since the original model of (Coon et al., 1974); namely the zero-tensile strength (ice is a

20 highly fracture material) and isotropy assumptions of the sea ice cover and rheological model. The use of continuum models such as the standard VP model for high-resolution simulations (1-10km) is also put in question since the grid size approaches a typical floe size and clearly violates the continuum assumption. For instance, recent high-resolution simulations using the VP model used spatial resolution of approximately $500\,\mathrm{m}$ for a regional domain (Wang et al., 2006) and $1\,\mathrm{km}$ for a pan-Arctic domain (Hutter et al., 2018a). While it can be argues that if the mode of deformation of a single floe is similar to that of an

25 aggregate of floes, a given rheology developed for a continuum can still be applicable at spatial resolutions of the order of the floe size Overland et al. (1998), the validity of a given flow rule across scales is not clear. Tsamados et al. (2013) included anisotropy explicitly in the VP model and show that it improved the representation of ice thickness and ice drift compared to an EVP model. Other VP sea ice rheology were also developed but were never widely used in the community. These include the coulombic yield curve with normal flow rule of (Hibler and Schulson, 2000), the lens, tear-drop, ice-cream cone,

30 diamond-shape yield curve with normal flow rules ((Zhang and Rothrock, 2005), the Mohr-Coulomb yield with double-sliding deformation law Tremblay and Mysak (1997); Ip et al. (1991); Flato and Hibler (1992).

Early work by (Marko John R. and Thomson Richard E., 1977) identified fracture lines (LKFs) in the pack ice and explained the presence of the LKFs by brittle fracture. Similar fracture patterns have also been observed from the centimeter scale in the lab, to hundreds of kilometers in satellite observations (Schulson, 2004; Weiss et al., 2007). Based on these (and others) satellite

35 observations and in-situ internal ice stress measurements, Weiss et al. (2007) proposed to model winter sea ice as a material that

undergoes brittle failure with subsequent sliding along LKFs governing inelastic deformations. Girard et al. (2011); Rampal et al. (2016); Dansereau et al. (2016) formalized the idea with the development of an Elastoc-Brittle (EB) and Maxwell-Elasto-Brittle (MEB) model with an additional parameterization to simulate damage associated with brittle fracture. We note that subsequent plastic deformations in this model are considered as elastic deformation (EB) or visco-elastic deformation (MEB)

5   instead of plastic. I.e. in the elastic approaches, the material does not weaken when fracture occurs, but rather the Young's modulus is reduced, leading to larger elastic deformations for the same stresses.Girard et al. (2009) compared the simulated sea-ice deformation fields from the EB and VP models with observations from the RADARSAT Geophysical Processor System (RGPS) and showed that the heterogeneity and the intermittency of deformation in the VP model are not consistent with observations. These results however could not be reproduced by other authors in the community. For instance, Spreen et al.

10 (2017); Hutter et al. (2018a); Bouchat and Tremblay (2017) all show that VP models are capable of simulating the PDFs of sea ice deformations over the whole Arctic in agreement with the same observations, when using appropriate shear and compressive strength of the material.

Similar fracture angles between intersecting LKFs 30±10°) were observed with different instruments (Landsat, Seasat/SAR, areal photographs,AVHRR) at different scales from 1 km to 100 km (Erlingsson, 1988; Walter and Overland, 1993). In the VP

15 model, LKFs are appear as line of high shear deformations. The weakening associated with the deformation results from divergence and reduction in ice concentration along the LKFs. This mechanism introduces anisotropy in high resolution simulations as seen in observations of comparable spatial resolutions. Previously fractured ice will be weaker and will affect future sea ice deformation fields. High-resolution sea-ice models simulate LKF patterns leads to anisotopy in the pack ice (Hutter et al., 2018a). Previous studies that looked at lead characteristics, including intersection angle between LKFs include (Hutchings

20 et al., 2005; Bröhan and Kaleschke, 2014; Lindsay and Rothrock, 1995; Wang et al., 2016; Hutter et al., 2018b). Of particular interest, Hutter et al. (2018b) compare LKFs and their intersection angles between RGPS data and a 2 km-model simulation similar to the one described in Hutter et al. (2018a). For the RGPS data, they find a broad distribution of intersection angles between LKFs that peaks around 20° (in line with previous assessments, e.g. Walter and Overland, 1993). The wide range of intersection angles is presumably due to previous deformation history and associated heterogeneity in the ice cover that dictates

25 the ice strength locally. Their results show a simulated distribution of intersection angles that is biased high with a modal value of 45° and with too few small intersection angles between 15 and 25°. The fact that a VP model overestimates the angles of intersection between LKFs is one motivation for the present thorough investigation of the fracture angles at small scales and the dependencies of the fracture angle to boundary conditions, model geometry, variability in sea in initial ice thickness field and mechanical strength parameters used in the model.

30   The simulation of fractures in sea ice models have been the focus of several previous studies using idealized model geometries. Hibler and Schulson (2000) investigated the effect of embedded flaws - that favors certain angles of fractures - in idealized experiments using a Coulombic yield curve. Hutchings et al. (2005) showed that LKFs can be simulated with an isotropic VP model using a idealized model geometry. The shape of the elliptical yield curve (ratio of shear to compressive strength) in the standard VP model has an impact on the presence or absence of ice arches in an idealized channel experiment (Dumont

35 et al., 2009). To build an anisotropic rheology, Wilchinsky et al. (2010) used a Discrete Element Model (DEM) model in an

idealized model domain and showed clear diamond-shaped fracture patterns. Idealized experiment are also used to investigate new rheologies (e.g. Dansereau et al., 2016; Sulsky et al., 2007, with the Maxwell-Elastic-Brittle (MEB) rheology, or the Material-Point Method (MPM)), or to study the theoretical framework explaining the fracture angles (e.g. Dansereau et al., 2017, with the Mohr-Coulomb yield curve in an MEB model). Recently, Heorton et al. (2018) compared simulated fractures

5 by the EVP and EAP models using an idealized model geometry and wind forcing, and showed that the anisotropic model creates sharper deformation features. To the best of our knowledge, the dependency of the fracture angles in sea ice on the shape of the yield curve using high resolution models has not yet been investigated. This is another motivation of this study.

In this paper, we explore the details of fracture with two VP rheologies using an idealized experiment at an unprecedented resolution of $25\,\mathrm{m}$.The remainder of this paper is structured as follow : Section 2 presents the experimental setup: the VP

10 framework (2.1), the definition of the yield curve (2.2), and the description of the idealized experiment (2.3). Section 3 presents the results : from the reference simulation (3.1), the effect of boundary conditions (3.3), the effects of lateral confinement (3.4), and the influence of heterogeneity (3.5). Furthermore, we consider the effects of two different yield curves with normal flow rule in subsection 3.6: the elliptical (3.6.1) and the coulombic yield curve (3.6.2). Discussion and conclusions follow in sections 4 and 5.

15 ## 2 Experimental Setup

2.1 Viscous-Plastic model

We use the Massachusetts Institute of Technology general circulation model (MITgcm, Marshall et al., 1997) with its sea ice package (Losch et al., 2010). All thermodynamic processes have been turned off for our experiments. The initial sea ice conditions – mean (grid cell averaged) thickness h and fractional sea ice cover A – are advected by ice drift velocities with a

20 third order flux limiter advection scheme. Ice drift is computed from the sea ice momentum equation

$$\rho h \frac{\partial \boldsymbol{u}}{\partial t} = -\rho h f \boldsymbol{k} \times \boldsymbol{u} + \boldsymbol{\tau}_{air} + \boldsymbol{\tau}_{ocean} - \rho h \nabla \phi(0) + \nabla \cdot \boldsymbol{\sigma}, \tag{1}$$

where ρ is the ice density, h is the grid cell average sea ice thickness, $\boldsymbol{u}$ is the velocity field, f is the Coriolis parameter, $\boldsymbol{k}$ is the vertical unit vector, $\boldsymbol{\tau}_{air}$ is the surface air stress, $\boldsymbol{\tau}_{ocean}$ is the ocean drag, $\nabla \phi(0)$ is the gradient of sea surface height, and σ is the vertically integrated internal ice stress tensor. The form of σ defines the rheology. In the case of the standard VP model

25 described in (Hibler, 1979), σ is defined as

$$\sigma_{ij} = 2\eta_{ij}\dot{\varepsilon}_{ij} + (\zeta - \eta)\dot{\varepsilon}_{kk}\delta_{ij} - \frac{P}{2}\delta_{ij}, \tag{2}$$

where δ_{ij} is the Kronecker delta and summation over equal indices is implied. η and ζ are the shear and bulk viscosities, $\dot{\epsilon}_{ij}$ is the strain rate tensor defined as

$$\dot{\epsilon}_{ij} = \frac{1}{2}\left(\frac{du_i}{dx_j} + \frac{du_j}{dx_i}\right), \tag{3}$$
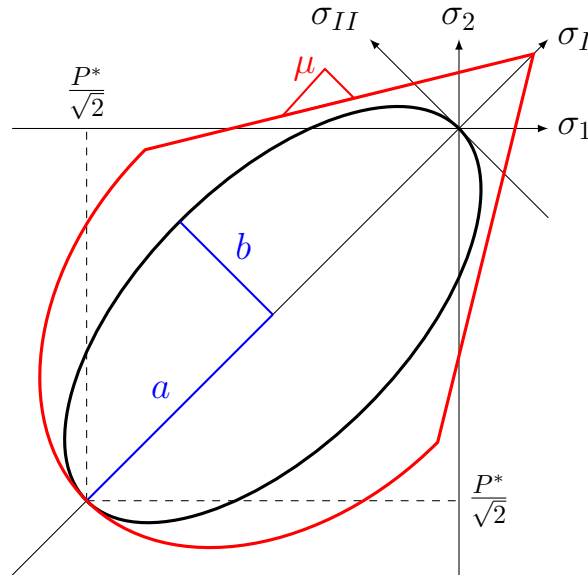
Figure 1. Example of yield curves used in VP models shown in : Ellipse with $e = 2$ in black , coulombic yield curve in red. μ is the slope of the Mohr-Coulomb flat on the coulombic yield curve as defined in equation (A5)

and P is the maximum compressive stress defined as a function of the mean sea ice thickness h and the sea ice concentration A:

$$P = P^* h\, e^{-C^*(1-A)}.$$ (4)

The values of parameters and constants in the model are given on Table 1.

2.2 Yield curve

When internal sea-ice stresses reach a critical value in compression, tension or shear, sea ice fails and relatively large plastic deformations are present. For internal ice stresses that are lower than the same thresholds, highly viscous (creeping) flow is present mimicking small reversible elastic deformations. Plastic deformations are relatively large and non-reversible. Viscous deformation are negligibly small and also non-reversible contrary to elastic reversible deformation in real sea ice. The yield criterion is expressed as a 2D envelope either in principal or stress invariant space with a normal flow rule - assuming that the principal stress and strain-rate axis coincide. The stress state on the yield curve together with the normal flow rule therefore determines the relative importance of divergence (positive or negative) and shear strain rate at a point. The magnitude of the deformation is such that the stress state remains on the yield cure during plastic deformation.

In this study, we use two different yield curves, the elliptical yield curve (Hibler, 1979) and coulombic yield curve (Hibler and Schulson, 2000) both with the normal flow rule. For the elliptical yield curve (in black in Figure 1), η and ζ are given by :

$$\zeta = \frac{P}{2\Delta}, \tag{5}$$

$$\eta = \frac{\zeta}{e^2}, \tag{6}$$

5   with the abbreviation

$$\Delta = \sqrt{(\dot{\epsilon}_{11} + \dot{\epsilon}_{22})^2 + \frac{1}{e^2}\left((\dot{\epsilon}_{22} - \dot{\epsilon}_{11})^2 + 4\dot{\epsilon}_{12}^2\right)} \tag{7}$$

where e is the ellipse ratio defined as

$$e = \frac{a}{b}. \tag{8}$$

where a and b are shown in blue on figure 1. The ellipse aspect ratio e defines the shear strength $S^\star$ of the material as a fraction
10   of its compressive strength: $S^\star = \frac{P^\star}{2e}$ (Bouchat and Tremblay, 2017). For the Coulombic yield curve, the shear viscosity η above is capped on the two straight limbs (see appendix A for a detailed derivation.

$$\eta_{MC} = \min\left\{\eta, \frac{1}{s}\left[\mu\left(\frac{P}{2} - \zeta \cdot \dot{\epsilon}_{kk}\right) - c\right]\right\} \tag{9}$$

with

$$s = \sqrt{(\dot{\epsilon}_{22} - \dot{\epsilon}_{11})^2 + 4\dot{\epsilon}_{12}^2} \tag{10}$$

15   The theoretical angle of fracture can be calculated from the generalized state of stress equations on a rotated frame of reference at an angle θ from a reference coordinate frame of reference. The stress tensor σ can be expressed in different sets of coordinates: in terms of principal stresses σ_1 and σ_2 and stress invariants σ_I and σ_{II}. The principal stresses σ_1 and σ_2 are the principal components or eigenvalues of the stress tensor on an sea ice element. Eigenvalues always exist, because the stress tensor is by definition symmetric. The principal stresses σ_1 and σ_2 can be expressed as a function of σ_{ij} as :

$$\sigma_1 = \frac{1}{2}\left(\sigma_{11} + \sigma_{22} + \sqrt{(\sigma_{11} - \sigma_{22})^2 + 4\sigma_{12}^2}\right), \tag{11}$$

$$\sigma_2 = \frac{1}{2}\left(\sigma_{11} + \sigma_{22} - \sqrt{(\sigma_{11} - \sigma_{22})^2 + 4\sigma_{12}^2}\right), \tag{12}$$

This change of coordinates can then be represented as a rotation of the coordinates of value ψ as shown on Figure A1. This angle, from Tremblay and Mysak (1997), is :

$$\tan(2\psi) = \frac{2\sigma_{12}}{\sigma_{11} - \sigma_{22}}. \tag{13}$$
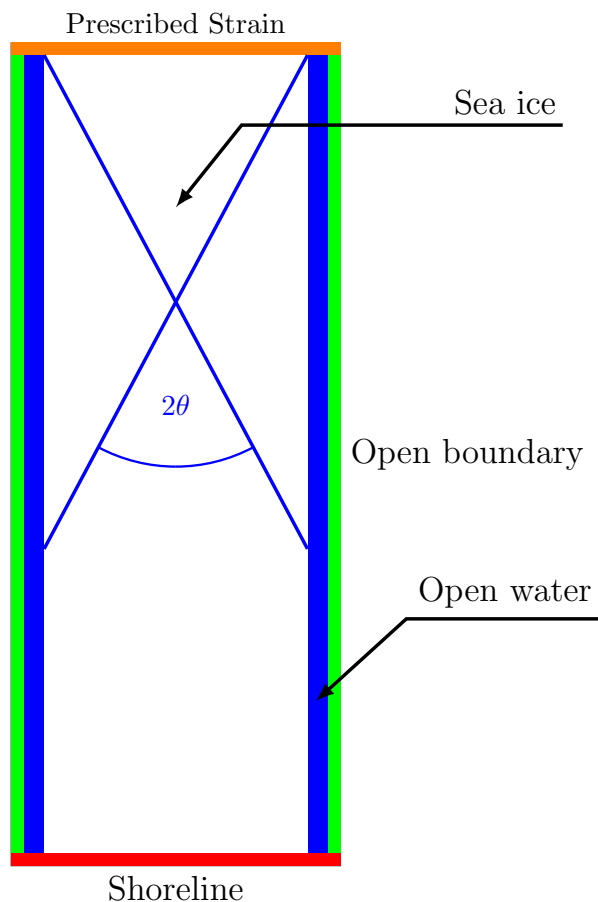
Figure 2. *Schematic of the experiment. The red area represent blocked grid cells, the green area is open boundary that let ice leave the domain with* von Neumann *boundary conditions. The orange area represent the prescribed area where the ice is forced with southward velocity. θ is the measured fracture angle with the blue line representing an LKF.*

Any linear combination of the principal stresses would be stress invariants. One commonly used definition called the stress invariants are the mean normal stress (σ_I) and the maximal shear stress (σ_{II}). They are expressed as function of stresses σ_{ij} or principal stresses σ_k as

$$\sigma_I = \frac{1}{2}(\sigma_1 + \sigma_2) = \frac{1}{2}(\sigma_{11} + \sigma_{22}), \tag{14}$$

$$5 \quad \sigma_{II} = \frac{1}{2}(\sigma_2 - \sigma_1) = -\frac{1}{2}\sqrt{(\sigma_{11} - \sigma_{22})^2 + 4\sigma_{12}^2}. \tag{15}$$

2.3 Idealized Experiment

An idealized uni-axial compressive test is used to investigate the modes of sea ice fracture (Figure 2). This experiment is standard in engineering (Schulson, 2004; Weiss et al., 2007) and also analogous to an experiment described in Dansereau et al. (2016) and Herman (2016). All experiments presented below use the same set-up unless specified otherwise. The values of parameters and constants are presented in Table 1.

The model domain is a rectangle of size $10\,\mathrm{km} \times 25\,\mathrm{km}$. An ice floe of size $8\,\mathrm{km} \times 25\,\mathrm{km}$, surrounded by $1\mathrm{km}$ of open water on the eastern and western sides, is compressed with a linearly (in time) increasing strain rate from the North against a solid Southern boundary. The open-water areas on the East and West boundary are used so that interesting dynamics are not influence by the choice of boundary conditions. We use a no-slip condition for the southern boundary, constraining the ice laterally. Note that the results presented below are robust of the choice of boundary condition on the east, west and south boundary. Because the simulation time and ice velocity are small, the Coriolis force in the momentum equations are neglected. The ocean and sea ice are initially at rest. The ice floe has a uniform concentration of 100% and thickness of $1\,\mathrm{m}$. The spatial resolution of the model is $25\,\mathrm{m}$. We use the Line Successive (over) Relaxation (LSR) solver to solve the sea ice momentum equations with 1500 non-linear iterations and 1500 linear iterations within each non-linear iteration (Zhang and Hibler, 1997; Lemieux and Tremblay, 2009). A high number of iterations is required because of slow convergence of the highly non-linear nature of the rheology term and the high spatial resolution (Lemieux and Tremblay, 2009). On the open eastern and western boundaries, we use von Neumann boundary conditions for velocity, thickness and concentration and ice can escape the domain unrestricted:

$$\left.\frac{\partial u}{\partial x}\right|_{E,W} = \left.\frac{\partial v}{\partial x}\right|_{E,W} = \left.\frac{\partial A}{\partial x}\right|_{E,W} = \left.\frac{\partial h}{\partial x}\right|_{E,W} = 0, \tag{16}$$

where E and W denote the Eastern and Western respectively. The ice is initially at rest. Strain is applied on the ice at the northern boundary by prescribing a velocity that increases linearly with time :

$$v|_N(t) = a_v \cdot t + v_i \ ; \ u|_N = 0 \ ; \ \left.\frac{\partial A}{\partial y}\right|_N = \left.\frac{\partial h}{\partial y}\right|_N = 0, \tag{17}$$

where a_v is the prescribed acceleration, and N denote the northern boundary.

3 Results

3.1 Uni-axial compressive test

In the reference experiment with default parameters, a diamond shape fracture appears in the shear strain rate and divergence fields after a few seconds of integration (Figure 3). The fracture appears right away but is visible in the deformation field only after a few seconds of integration. The shear deformation ($\dot{\epsilon}_{II}$) shows where the ice slides in friction and deforms plastically. From Figure 3, the measured intersection angle is $\theta = 33.8 \pm 0.5°$. All angles measured in this study have an error range around $1\mathrm{deg}$. Because we model an oblique fracture on a grid, the size of the grid spacing spread the deformation line, and the fracture spread on several pixels because of the obliquity of the fracture.

Table 1. Model parameters for the reference simulation

Symbol	Definition	Value	Unit
ρ	Density of ice	910	$\mathrm{kg\,m^{-3}}$
$P^\star$	Ice strength	27.5	$\mathrm{kN\,m^{-1}}$
C	strength reduction parameter	20	
dx, dy	Grid Spacing	25	m
C_w	Water drag coefficient	5.21×10^{-3}	
N_x, N_y	Size of the Domain	400×1000	
L_x, L_y	Size of Experiment	10×25	km
l_x, l_y	Ice floe's size	8×25	km
A	Ice Concentration	100	%
h	Ice Thickness	1.0	m
N_{lin}	Nbr. Linear Iteration	1500	
N_{nlin}	Nbr. Non-linear Iteration	1500	
ϵ_{err}	Max. error in LSR	10^{-11}	
dt	timestep	0.1	s
e	ellipse ratio (a/b)	2.0	
v_i	initial velocity	0	$\mathrm{m\,s^{-1}}$
a_v	acceleration	$5 \cdot 10^{-4}$	$\mathrm{m\,s^{-2}}$

Results after a few time steps show lower (or equal) ice thickness in the model domain, particularly along the LKFs (Fig. 3, middle panel) where divergence is present. Note that the loading axis in our simple 1D experiment is also the second principal axis and consequently the stress states are slowing migrating along the σ_1 axis as the strain rate at the northern boundary increases. Fracture occurs when the stress state intersects the yield curve; this occurs in the first half of the ellipse (for $e < 1$)

5 where the normal to the flow rule points in the positive divergence (or first strain rate invariant) direction (see Figure 4). This explains the simulated divergent flow field and lower ice thickness particularly along LKFs.

The results presented above are robust with respect to the spatial resolution and model domain size (see Figure 5).

3.2 Fracture and generation of smaller floes

Here, the reference simulation is extended for a longer time period (2700 seconds or 45 min), using a smaller number of nu-

10 merical iterations because of computational constraints (150 iterations instead of 1500 for both linear and non-linear iterations with the LSR solver, see Figure 6). The ice floe is broken into separated ice floes of smaller diamond-scale. The openings are visible in the thickness and concentration fields with thinner ice in the lead. Contrary to the previous short experiment, the sea ice ridged at several points and thickness increases, especially in the center of the central diamond, where the tip of the
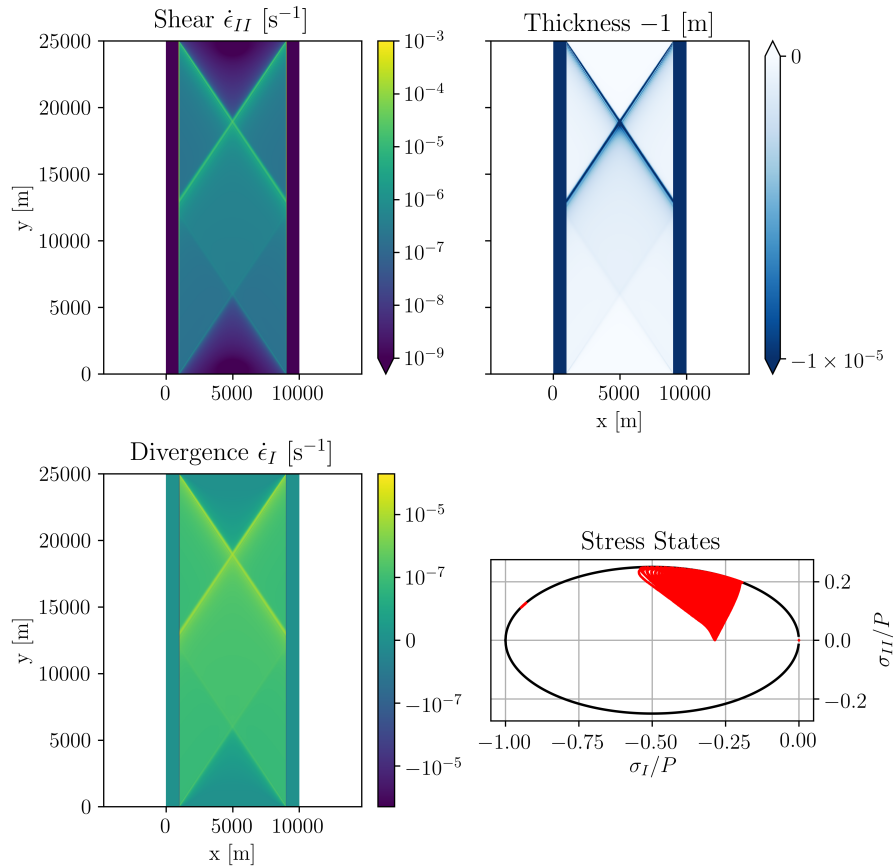
Figure 3. Results of the reference simulation after 10 seconds of simulation. **Top left:** Shear deformation inside the ice floe, showing a diamond shape fracture. **Bottom left:** Divergence deformation inside the ice floe, showing the divergence in the fracture line that lead to an opening. **Top right:** Modification of the thickness compared to initial state of 1 m, the opening with a diamond shape is visible. **Bottom right:** Stress states in red, with the elliptical yield curve in black.

upper triangle is compressed. There is also some thicker ice at the northern boundary because of the boundary condition. The fracture into several floes that move independently on open-water at this resolution appears realistic. Several fractures develop in parallel similarly as the comb crack or secondary fault lines, described in Schulson (2004).

3.3 Effects of no-slip boundary condition and geometry

5   The dynamics presented above are happening away from the east/west boundaries. We now investigate the robustness of the results to the choice of southern boundaries. To this end, we reduce the domain size to $10\,\mathrm{km} \times 10\,\mathrm{km}$ with an ice floe of $8\,\mathrm{km} \times 10\,\mathrm{km}$ in the interior, in such a way that the ice fracture ends on the southern boundary where a no-slip boundary condition is imposed - as opposed to the east/west boundaries as presented above. In this case, the fracture develops from
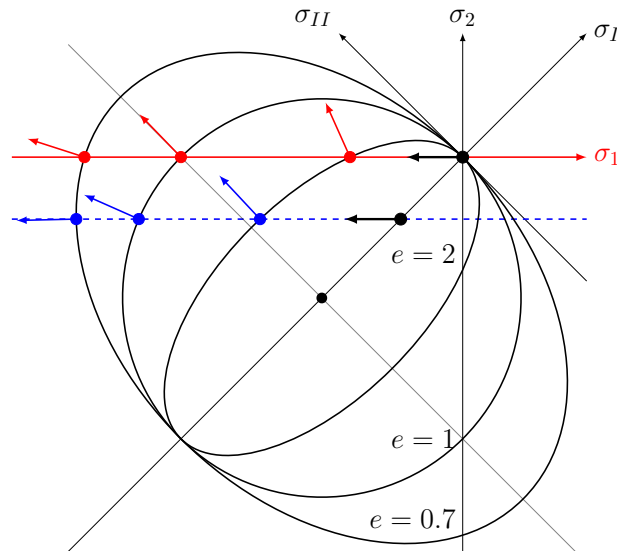
Figure 4. Schematic of stress state migration during uni-axial loading experiments. Red arrows shows the stress state at fracture – the intersection point between the second principal axis σ_1 (in red) and the elliptical yield curve – for different ellipse ratio: $e = 2$, $e = 1$, and $e = 0.7$. The blue arrows show the case when the ice floe is confined. The stress states migrate from a point with a higher compressive stress.
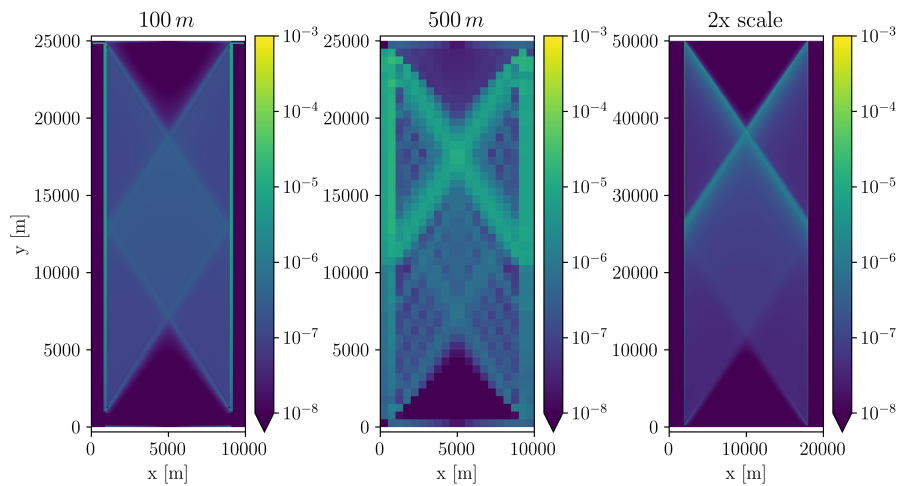
Figure 5. Shear deformation (or $\dot{\epsilon}_{II}$) after $2\,\mathrm{s}$ with **(left)** a coarser resolution of $100\,\mathrm{m}$, **(middle)** a coarser resolution of $500\,\mathrm{m}$ and **c)** in a experiment with a domain that has been doubled in both directions to a size of $20\,\mathrm{km} \times 50\,\mathrm{km}$ at resolution of $25\,\mathrm{m}$, with a doubled prescribed velocity to keep deformation rate constant.

corner to corner and the angle is solely determined by the geometry of the ice floe, that is, $\theta = \arctan(l_x/l_y)$ (right hand side of Fig. 7 shows an example). With free-slip boundary condition on the South boundary, the fracture angle is similar to the one
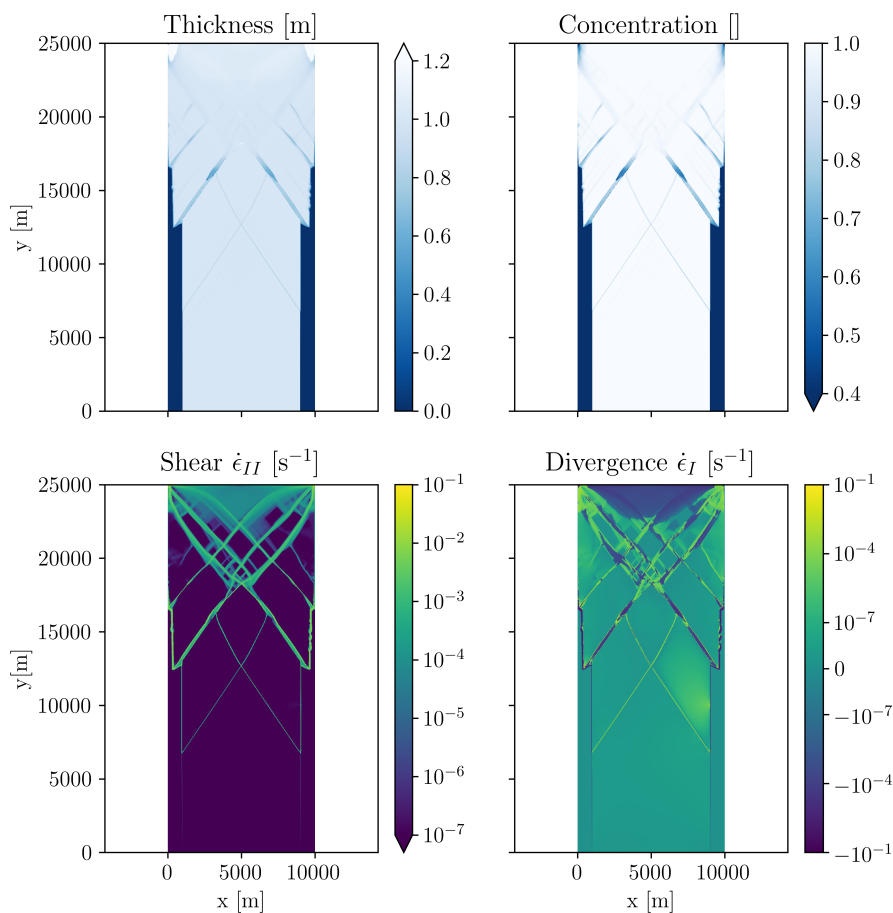
Figure 6. Uni-axial compressive test after 2700 s (45 min). Results show the primary and secondary fracture lines**(top left)**: sea ice thickness; **(top right)**: sea ice concentration; **(bottom left)**: shear strain rate $\dot{\epsilon}_{II}$; **bottom right**: divergence $\dot{\epsilon}_I$

.

of the reference simulation (left hand side of Figure 7). I.e. the no-slip condition acts as a stress concentrator on the corner of ice floe and pre-determines the fracture location. A slip boundary condition is therefore considered more physical in such idealized experiments.

No-slip or free-slip boundary conditions have little impact on the fracture angle in the larger reference domain with longer floe, because the LKFs always end on the open-water boundaries of the floe (not shown). With the free-slip boundary conditions, the stress and strain are only different south of the diamond fracture pattern because ice can move along the southern boundary and the second fracture cannot form.
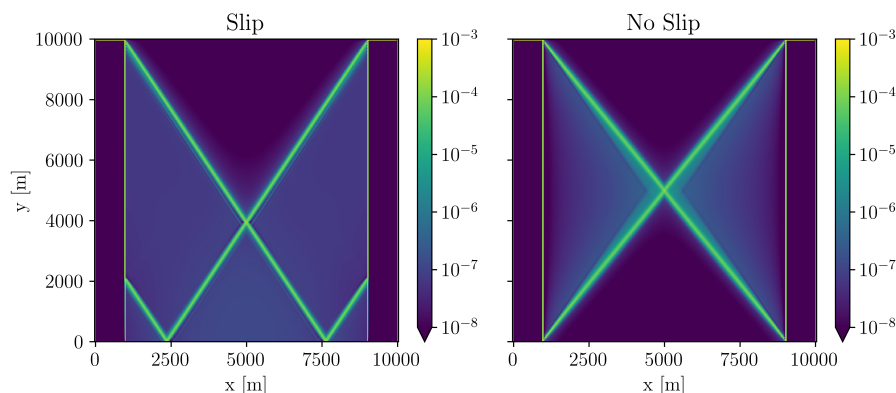
Figure 7. Snap shot of shear strain rate after $15\,\mathrm{s}$ with a reduced-size ice floe of $8\,\mathrm{km} \times 10\,\mathrm{km}$) **(left))** with a slip boundary condition on the southern boundary, $\theta = 33.8° \pm 0.5$, and **(right)** with a no-slip boundary condition, $\theta = 39° \pm 0.5$.

3.4 Effects of lateral confinement

We explore the effect of confining pressure on the eastern and western boundaries on the angle of fracture. To do so, we introduce solid walls on the eastern and western boundaries of the domain (similar to the southern boundary) and fill the open water gap between the ice and wall with ice of different thicknesses h_c. As the strength of sea ice increases linearly with
5   thickness, the fracture angle changes depending on the thickness of the surrounding ice.

With an increasing lateral confinement (blue curve in Figure 4) the fracture angle increases (Figure 8). The deformation points are migrating towards higher compressive stresses on the yield curve. As the ice is under pressure on the eastern and western boundaries, it cannot move freely eastward and westward so that it then enters the ridging phase more readily. With increasing confinement, the stress states of the ice floes move to more negative values of σ_1 along a $\sigma_2 = constant$ line (blue
10   line in Figure 4) with deformation moving towards more convergent states. Between $h_c = 0.2$ and $h_c = 0.3$, the regime changes from lead opening to ridging, as the fracture angle pass above $45°$.

3.5 Effects of the heterogeneity

Local weaknesses in the initial ice field also has an effect on the fracture angle. When weaknesses are embedded in the initial ice field, failure occurs first at this points. This lead to a stress concentration which raises the stress level and causes failure.
15   This in turn raises the stress level in the adjacent grid cell and crack propagation proceeds in this manner. In this case, the fracture links stress concentrators together to form a fracture and the angle of fracture is determined also by the distribution of initial ice weaknesses rather than only by the shape of the yield curve or mechanical stress parameters. Figure 9 shows an initial ice thickness field with two areas of lower ice thickness, hence weaker ice (left hand side), and the results of two simulations after $50\,\mathrm{s}$, with $e = 2$ (middle) and $e = 1$ (right hand side). The fracture patterns are very different from the reference case as
20   the fracture lines now start or terminate at the corners of the weak ice areas. Still, changing the yield curve by means of e
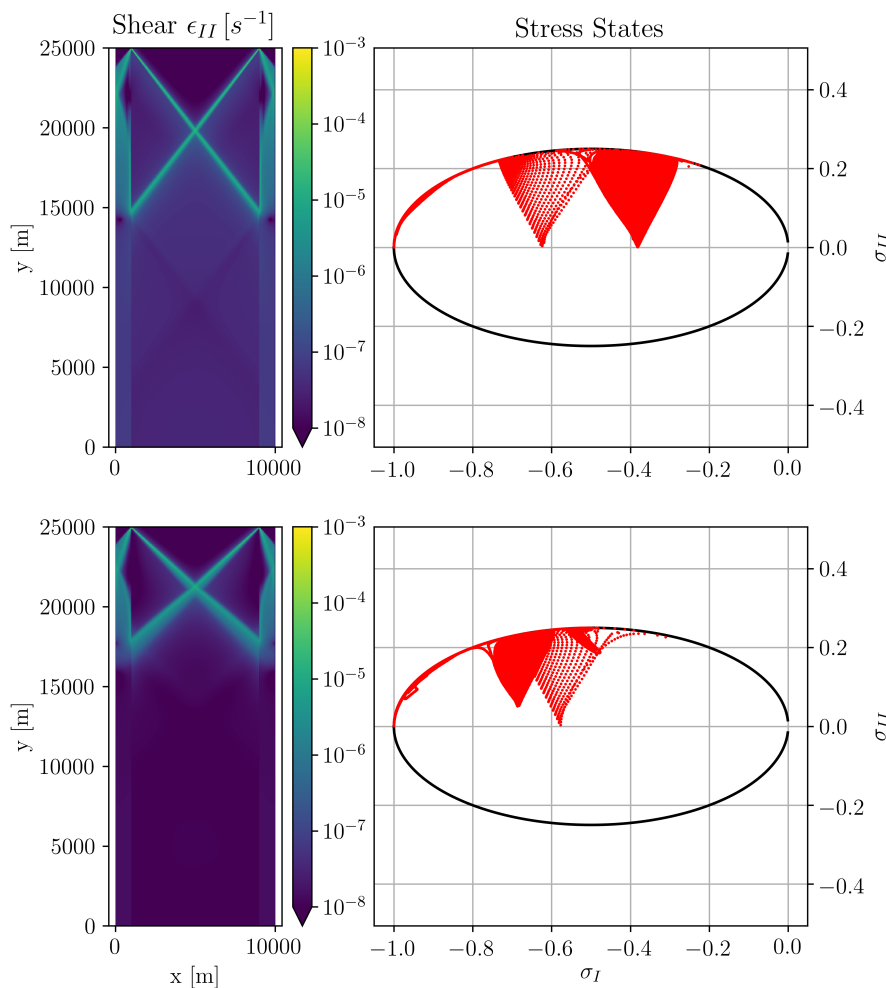
Figure 8. Shear strain and stress states for **(Top)** $h_c = 0.05\,\mathrm{m}$ and **(Bottom)** $h_c = 0.3\,\mathrm{m}$ after 5 seconds of simulation.

changes the fracture pattern. The weakness influences the fractures resulting in angles different than expected for these yield curve settings in both cases. Nevertheless, the two fractures are different as the yield curve has an impact on the preferred fracture angle. With $e = 1$, the angles are much wider compared to $e = 2$ (see section 3.6.1 below).

3.6 Effects of the yield curve on the fracture

5 #### 3.6.1 Elliptical yield curve

The idealized experiment are repeated changing only the ellipse ratio e. Thus, the maximal shear strength $S^\star$ increases or decreases while the maximal compressive strength $P\ast$ remains constant at $27.5\,\mathrm{kN\,m^{-1}}$. Scaling the absolute values of $P^\star$ and $S^\star$ while keeping e constant does not change the fracturing pattern (not shown). Changing the ellipse aspect ratio e, however,
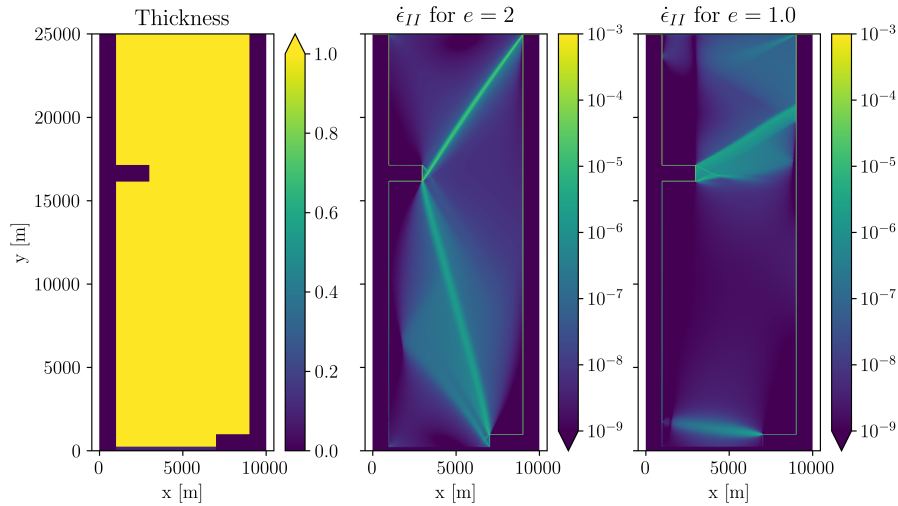
Figure 9. (left) Initial ice thickness with two weak areas of lower ice thickness. Shear strain rate $\dot{\epsilon}_{II}$ after 5 seconds with **(middle)** $e = 2$ and **(right)** with $e = 1$.
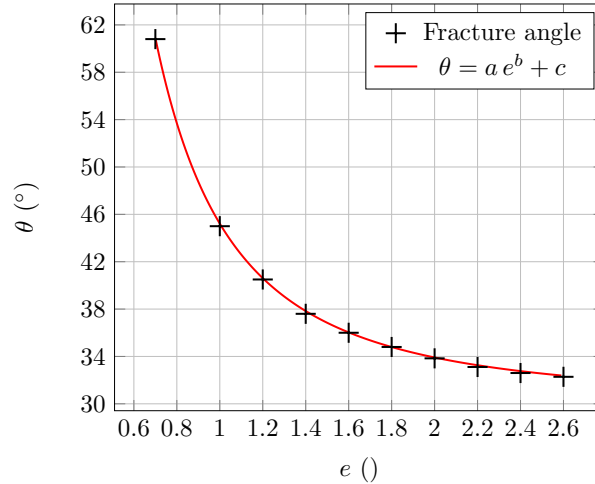
Figure 10. Fracture angles as a function of ellipse aspect ratio e with constant P^*. The red curve fits the data with $a = 15.1$, $b = -1.96$, and $c = 29.9$. The R-square value of the fit is $R^2 = 0.9997$ and the standard-deviation value is $\sqrt{\sigma} = 0.0639$. Rounding the value to 2 significant numbers, we get the parameters, $a = 15$, $b = -2$, and $c = 30$. These rounded values still give an excellent fit with $R^2 = 0.9995$ and $\sqrt{\sigma} = 0.089$. The simulated fracture angle as function of e becomes $\theta = \frac{\pi}{6} + \frac{\pi}{12}e^{-2}$ when expressed in radians.

has a large effect on the fracture angle. The fracture angle decreases monotonically as the shear strength of the material (or e) decreases, from $60.9°$ for $e = 0.7$ to $32.3°$ for $e = 2.6$. An empirical function $\theta = \frac{\pi}{6} + \frac{\pi}{12}e^{-2}$ can fit the data points and
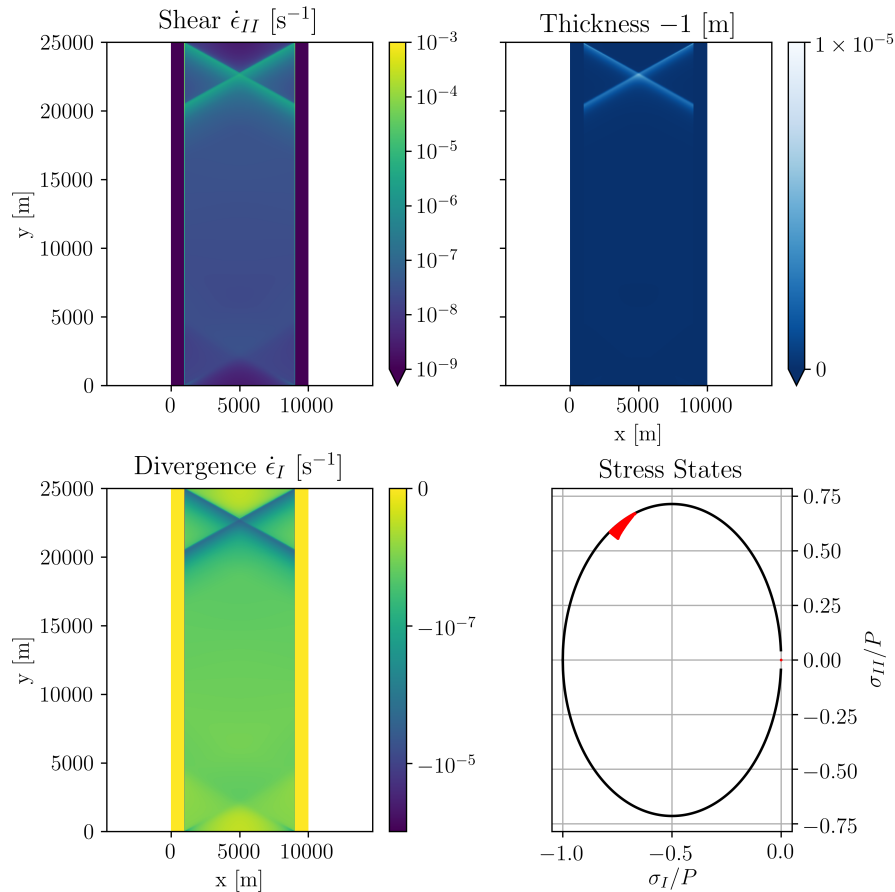
Figure 11. After 5 seconds of simulation with $e = 0.7$. **Top left:** Shear deformation inside the ice floe, showing a diamond shape fracture. **Bottom Left:** Divergence deformation in the floe, showing the convergence zone at the fracture location, leading a ridging event. **Top right:** Modification of the thickness compared to initial state of 1 m, the ridging with a diamond shape is visible. **Bottom right:** Stress states in red, with the elliptical yield curve in black.

is presented on Figure 10. This is in contrast with the behaviour of other granular materials with an angle of fracture that decreases with increasing shear strength or cohesion.

   Bouchat and Tremblay (2017) suggest the use of a smaller ellipse aspect ratio (e.g. $e = 0.7$) to obtain a closer match with radarsat-derived distribution of deformation rates in pan-Arctic simulations at 10 km resolution. From Figure 10 and 11, the corresponding fracture angle is $\theta = 60.9°$; i.e. much larger that what is derived from radarsat images. e also changes the distribution of the stress states on the yield curve. As the stress state migrates along the principal stress σ_1 until it reaches the yield curve in uni-axial compressive test, for $e < 1$, the stress state are in the second half of the ellipse and the resulting deformation are in convergence (or ridging). The ice thickness increases due to ridging along the shear lines (Figure 11). In a longer simulation with $e = 0.7$ (not shown) the ice does not open but only ridges, with thickness building up within the ice

floe. This is in strong contrast to the results with $e = 2.0$ presented in Section 3.2 above where the initial floe breaks up and individual ice floes form.

3.6.2 Coulombic yield curve

In this section, we report results from a Coulombic yield curve with normal flow rule Hibler and Schulson (2000). This yield

5 curve consist of a Mohr-Coulomb failure envelope (two straight lines in principal or stress invariant space), capped by an elliptical yield curve for high compressive stresses. For a Mohr-Coulomb yield curve, the fracture angle depends directly on the slope of the Mohr-Coulomb envelope. (Appendix A).

   The slope of the modified yield curve μ is varied between 0.3 and 1.0 to study the dependency of the fracture angle to the shear strength of the material. In all experiments with the Coulombic yield curve, We use a tensile strength of 5% of P* and an

10 ellipse ratio $e = 1.4$, similar to Hibler and Schulson (2000). The tensile strength is introduced mainly for numerical reasons. With zero tensile strength, the state of stress in a simple uni-axial compressive test with no confinement pressure, is tangential to the yield curve at the origin (failure in tension) and on the two straight limbs (failure in shear), resulting in instabilities. With tensile stress (or confinement pressure) included, the state of stress reaches the yield only on the two limbs of the yield curve.

   Figure 12 shows the shear field and stress states for $\mu = 0.7$, $\mu = 0.85$, and $\mu = 0.95$ after 5 seconds of simulation. We

15 observe that the fracture pattern is very sensitive to μ. This makes a measuring the fracture angle difficult. We observe four different regimes :

$\boldsymbol{\mu} \simeq 0.3 - 0.5$ **(not shown here):** Sea ice shear strength is small for small stresses, deformations appear at the border of the ice with high values of deformation. A lot of small LKFs develop but no large fractures appear through the ice floe.

$\boldsymbol{\mu} \simeq 0.5 - 0.8$**:** The deformation takes place almost exclusively in the flat Mohr-Coulomb part of the yield curve. A distinct

20   fracture patterns is present, similar to the elliptical case. For $\mu = 0.7$, $\theta = 23.5 \pm 2°$ while the Mohr-Coulomb theoretical angle is$\theta_{MC}(\mu) = 22.6°$ from Eq. A9. (Top of Figure 12)

$\boldsymbol{\mu} \simeq 0.8 - 0.9$**:** The fracture structure is chaotic. The fracture lines are broad and have an inner structure that seems to be composed of two different angles. The deformation occurs on both parts of the yield curve, Mohr-Coulomb straight limbs and the elliptical cap; presumably, the poor definition of the fracture lines is due to the fact that the stress state

25   touches the yield curve on both part of the yield curve. For $\mu = 0.85$, fractures angles range around $28° \pm 2$.(Middle of Figure 12)

$\boldsymbol{\mu} \simeq 0.9 - 1.0$**:** The fracture pattern corresponds to the elliptical yield curve of $e = 1.4$, slightly modified by the 5% tensile strength (not investigated in this paper). Deformation states are on the elliptical part of the modified yield curve. With $\mu = 0.95$, the modeled fracture angle is $\theta = 40.9°$. (Bottom of figure 12)
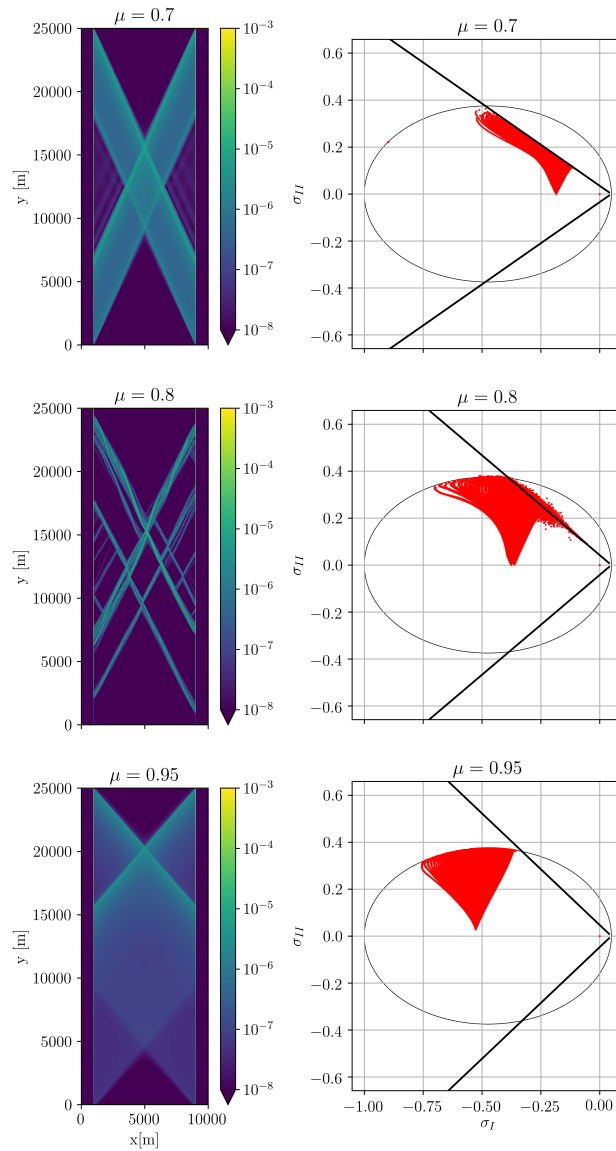
Figure 12. Shear strain $\dot{\epsilon}_{II}$ and stress states in simulation with e=1.4 after 5 seconds of simulation : **(top)** $\mu = 0.7$ and $\theta = 23.5°$, **(middle)** $\mu = 0.85$ and $\theta \simeq 28$ in average, and **(bottom)** $\mu = 0.95$ and $\theta = 40.9°$

4 Discussion

Our idealized experiment using the VP rheologies resolve LKFs as described by Hutchings et al. (2005) and akin to observations (Kwok, 2001). The fracturing of the ice floe creates smaller floes in a realistic manner. At the high resolution of 25 m the original interpretation of the continuity assumption, namely that that each grid cell should represent a distribution of floes (Coon et al.,

1974), is no longer valid. Instead, the emerging discontinuities and the polygonal diamond shape of the structures that appear as floes spanning many grid cells are a consequence of the mathematical characteristics of the VP model (Pritchard, 1988). Diamond shaped floes are observed in the Arctic ocean (Erlingsson, 1988; Walter and Overland, 1993) and also modeled using a Discrete Element Model (DEM) in an idealized experiment (Wilchinsky et al., 2010). Heorton et al. (2018) compared the

5   Elastic Viscous Plastic (EVP) rheology (Hunke and Dukowicz, 1997) to the Elastic Anisotropic Plastic (EAP) rheology, based on the diamond shape property of sea ice (Wilchinsky and Feltham, 2006). They found that EAP creates sharper fractures than the EVP model and find different regimes of fracture for different convergent and divergent wind forcing. Therefore the anisotropic model may improve the fracturing process for sea ice, especially by creating areas of oriented weaknesses, and particularly at coarse resolution where the fracture is not resolve by the grid spacing. In the high-resolution experiments

10   presented here, the VP rheologies appear to model sharp fracture lines.

    Other experimental choices have been explored to separate the effects of various parameters on the rheology. The fracture lines do not depend on' the experiment's resolution and scale. Thus, the rheology is shown to be scale independent, at least on the scales explored here, in line with observations (Schulson, 2004). Our results show that the no-slip boundary condition has little effect on the fracture pattern within our setup. However, the results suggest that in basin-wide simulations the choice

15   of boundary conditions affect the fracture depending on the geometry and stress direction. The no-slip condition appear to be unphysical and is acting on the stress concentrator on the corner and forcing the fracture to occur at this location, calling for an investigation of the boundary conditions for the shorelines. Similar results were obtained from analytical solutions in idealized geometry for the Morh-Coulomb yield curve with double sliding deformation law (Sirven and Tremblay, 2014). Confining the ice floe by thinner ice instead of open-water moves the stress states to higher compression and increases the fracture angle.

20   Therefore, we conclude that by surrounding our floe with open-water, we get the most acute angles from the rheology in this uni-axial compression setup. This is contradiction with the behavior of typical granular material that have an angle of fracture that is independent of the confining pressure (Hutter and Rajagopal, 1994). A heterogeneous ice cover shows changes in the fracture pattern. LKFs link the weaknesses in the ice cover, but the pattern still depends on the preferred fracture angles implied by the model rheology. In summary, we are confident that the our choice of parameters allows us to isolate the effects of the

25   rheology and the yield curve on the fracturing process.

    In granular material, large shear resistance is linked with contact normals between floes that oppose the shear motion and leads to dilatation (or divergence). In contrast, our experiment show that adding shear strength in the standard VP model (reducing the ellipse aspect ratio e) increases the fracture angle instead. This is contrast with the behavior of the granular material that show a decrease in fracture angle for larger shear strength (think of a wet sand castle versus a dry sandcastle). In

30   addition, high shear strength leads to convergence along the fracture plane whereas observations (e.g. radarsat deformations) show a range of positive and negative divergence along LKFs, again contrary to the results obtained with the standard VP model. Inspection of the stress states in the 2D stress plane suggests that the intersection of the yield curve with the σ_1 axis has an important role in the fracture process. This intersection point appears to determine the fracture angle, but the precise process that determines the fracture angles is unclear. In spite of this, our experiments allow to determine an empirical relationship

35   between the fracture angles and the ellipse ratio e. Sea ice simulation have been improved by decreasing the value of e, thereby

adding shear and bi-axial tensile and compressive strength (stress states with σ_1 or σ_2 positive, but not both), in Arctic-wide simulations (Miller et al., 2005; Dumont et al., 2009; Bouchat and Tremblay, 2017). Our results, however, show that this would make fracture angles larger, which is in stark contrast to what we expect to be necessary to improve the model.

The sea ice opening and ridging depending on the deformation states is consistent with the theory of the yield curve analy-
5   sis developed in Pritchard (1988). Interestingly, a change of ice maximum compressive strength $P^\star$ with a constant e has no influence on the LKF creation, although $P^\star$ is usually thought of as the principal parameter of sea ice models in climate simulations (e.g. Schmidt et al., 2014). The effects of bi-axial tensile strength $T^\star$ on fracture processes require further investigation, especially given the fact that the assumption of zero-tensile strength is being questions (Coon et al., 2007). The ice strength parameter $C^\star$ (The parameter governing the change of ice strength depending on ice concentration, equation 4) was not studied
10   here, although it appears to be an important tuning parameter and helps to improve basin-wide simulations (Ungermann et al., 2017).

With the coulombic yield curve, we can reduce the modeled fracture angle. The observed fracture angle with $\mu = 0.7$ is close to the $\simeq 20°$ described in Hibler and Schulson (2000), and corresponds to the theoretical framework described in Appendix A. Erlingsson (1988) developed another Mohr-Coulomb theory linking internal angle of friction and fracture angle. This complex
15   theory take into account the fractal (or self-similar) nature of sea ice. It gives different results, but is inadequate for a single ice floe simulated as presented here. The yield curve use here features a normal flow, while Weiss et al. (2007) shows that the deformations have an non-normal flow using in-situ measurements. With the normal flow rule on a Mohr-Coulomb yield curve, the ice only fracture in opening, which is non-physical because sea ice also forms ridges during compressive deformations. The effects of another flow rule may be investigated, for example a double-sliding law (Balendran and Nemat-Nasser, 1993;
20   Tremblay and Mysak, 1997).

5   Conclusions

Motivated by the observation that the intersection angles in a 2 km Arctic-wide simulation of sea ice are generally larger than in the RGPS dataset, the fracturing of ice under compression was studied with two VP rheologies in a highly idealized geometry and with very small grid spacing of 25 m. The main conclusions are:
25   The fracturing process in a ice floe of 8 km by 25 km is independent of the experiment resolution and scale, but sensitive to lateral boundary conditions (no-slip or free-slip). The fracture angle is also sensible to the surrounding sea ice cover, in contradiction with the granular nature of sea ice. The model produces a fracture opening with a diamond shape, and several smaller ice floes develop from the initial fracture. Unsurprisingly, the yield curve plays an important role in fracturing sea ice. Increasing the maximum shear strength in the sea ice model increases the fracture angle in contrast to expectations. Even if
30   the fracture process is not fully explained, we find an empirical relationship between fracture angle and the ellipse ratio e of the elliptical yield curve: $\theta \simeq \frac{15}{e^2} + 30$. Therefore, fracture angles below $30°$ are not possible with an elliptical yield curve. In this fully compressive setup, the divergence and convergence at the fracture line appear to be dependent in the shear strength of the ice, linked to the normal flow rule. The ice open and create leads with an ellipse ratio below $e = 1$, and ridge in the

inverse case. Using a modified coulombic yield curve, the fracture angle can be decreased, but the non-differentiable shape of this yield curve introduces numerical issues and an unclear fracture pattern in some cases. Therefore, non-differentiable yield curves (with a normal flow rule) should be avoided in viscous-plastic sea ice models.

5   The idealized experiment of a uni-dimensional compression is useful to explore the effects of the yield curve because all other parameters are controlled. Historically, the discrimination between the different yield curve couldn't have been done because of the scarcity of sea ice drift data. The recent sea ice deformation dataset from RADARSAT also, through LKFs statistics, indicated that we would need to increase the shear strength with the ellipse in the standard VP rheology to match observations. This would increase the fracture angles, in opposition to the needed improvements. Therefore, the high-resolution idealized experiment presented in this work gives means to investigate and discriminate different rheologies – yield curve and

10   flow rule.

If Arctic-wide sea ice simulations with a resolution of $25\,\mathrm{m}$ are not feasible today because of computational cost, we can still imagine such a model to be useful for process modeling on small scales, for example, to constrain the rheology with data from the upcoming MOSAiC scientific cruise (Dethloff et al., 2016) that will provide a full year of sea ice observations in pack ice. Such simulations would also need to take into account the effects of heterogeneous ice cover and wind patterns, with

15   potentially convergent and divergent forces from the wind. Most climate models use the standard VP rheology (Stroeve et al., 2014) or one of its variants (e.g. EVP). Results presented here however points at the need for a more physical yield curve and (non-associative) flow rule. A better understanding of the link between the fracture process and the yield curve and the flow rule is necessary for more confidence in the capacity of the rheology to model sea ice dynamic in a consistent way. Once the fracture process within the VP framework is fully understood, the design of a new yield curve, including a different flow rule,

20   that would take into account the granular nature of sea ice and be adapted to high resolution modeling and LKFs creation appears to be necessary.

Appendix A: Fracture angle

We follow Hibler and Schulson (2000) and Tremblay and Mysak (1997) to derive a relationship between the fracture angle and the internal angle of friction for the Mohr-Coulomb curve. The stresses on a plane at an angle θ from the principal stress axis

25   (σ_1, σ_2) can be written as (see Figure A1 and Popov (1976))

$$\sigma dA = \sigma_2 \sin(\theta)\sin(\theta)dA + \sigma_1 \cos(\theta)\cos(\theta)dA, \tag{A1}$$

$$\tau dA = \sigma_2 \cos(\theta)\sin(\theta)dA - \sigma_1 \cos(\theta)\sin(\theta)dA, \tag{A2}$$

where dA is the area of the friction plane. Simplifying using trigonometry relationships, we can write the stress σ and τ in terms of the stress invariants σ_I and σ_{II}

30   $$\sigma = \sigma_I + \sigma_{II}\cos(2\theta), \tag{A3}$$

$$\tau = \sigma_{II}\sin(2\theta). \tag{A4}$$
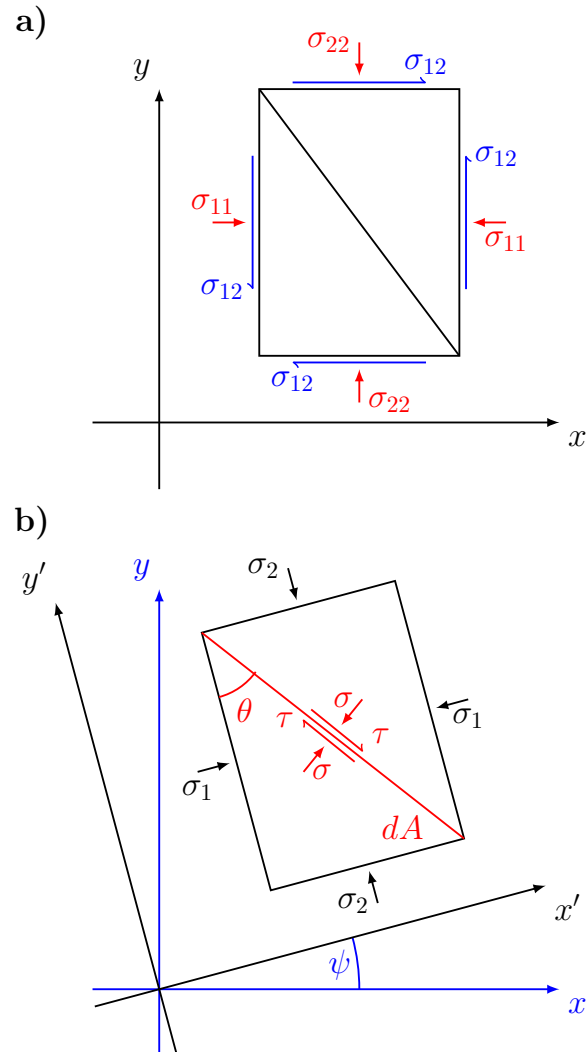
Figure A1. Stress state on an ice element in the reference σ_{ij} **a)** or in principal stress space (σ_1,σ_2) and along an arbitrary inclined plane at an angles θ **b)**. The principal axis are the eigenvalues of the stress tensor and the angle ψ comes from the rotation matrix composed of the eigenvectors.

The Mohr-Coulomb failure criterion can be written in the reference stress space (see Figure A2)

$$\tau = -\tan(\phi)\,\sigma + c, \tag{A5}$$

where ϕ is the internal angle of friction, and c the cohesion when no stress is applied. Substituting (A3) and (A4) in (A5) we get

5 $\quad -\sigma_{II}\sin(2\theta) = \tan(\phi)\,\sigma_I + \tan(\phi)\,\sigma_{II}\cos(2\theta) + c. \tag{A6}$
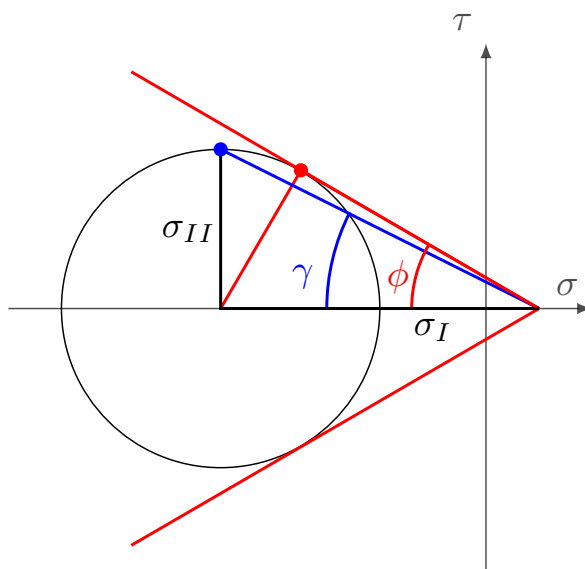
Figure A2. Mohr-Coulomb circle of stress in an arbitrary frame of reference at an angle θ with the respect to the principal stress. $\tan(\gamma) = \mu$, the slope if the blue line.

that we develop as

$$\sigma_{II}\left(\sin(2\theta)\cos(\phi) + \cos(2\theta)\sin(\phi)\right) = -\mu\sigma_I + c \tag{A7}$$

where we have used the fact that $\mu = \tan(\gamma) = \sin(\phi)$ (see Figure A2), where μ is the coefficient of internal friction. This then imply that in invariant space (σ_I, σ_{II})

5   $$\sin(2\theta)\cos(\phi) + \cos(2\theta)\sin(\phi) = 1 \tag{A8}$$

   Therefore we get

$$\theta = \frac{\pi}{4} - \frac{\phi}{2} = \frac{\pi}{4} - \frac{\sin^{-1}(\mu)}{2} \tag{A9}$$

Author contributions. Damien Ringeisen designed the experiments, ran them, and interpreted the results with help from Martin Losch and Bruno Tremblay. Nils Hutter contributed to the discussion with his insights on LKFs in simulations and observations. Damien Ringeisen

10   prepared the manuscript with contributions from all co-authors.

Competing interests. The authors declare that they have no conflict of interest.

Acknowledgements. This project was supported by the Deutsche Forschungsgemeinschaft (DFG) through the International Research Training Group "Processes and impacts of climate change in the North Atlantic Ocean and the Canadian Arctic" (IRTG 1904 ArcTrain).

The authors would like to thank the Isaac Newton Institute for Mathematical Sciences for support and hospitality during the program Mathematics of sea ice phenomena when work on this paper was undertaken. This work was supported by: EPSRC grant numbers EP/K032208/1

5   and EP/R014604/1.

(c) Author(s) 2018. CC BY 4.0 License.

References

Balendran, B. and Nemat-Nasser, S.: Double sliding model for cyclic deformation of granular materials, including dilatancy effects, Journal of the Mechanics and Physics of Solids, 41, 573–612, https://doi.org/10.1016/0022-5096(93)90049-L, http://www.sciencedirect.com/science/article/pii/002250969390049L, 1993.

5 Bouchat, A. and Tremblay, B.: Using sea-ice deformation fields to constrain the mechanical strength parameters of geophysical sea ice, Journal of Geophysical Research: Oceans, pp. n/a–n/a, https://doi.org/10.1002/2017JC013020, http://onlinelibrary.wiley.com/doi/10.1002/2017JC013020/abstract, 2017.

Bröhan, D. and Kaleschke, L.: A Nine-Year Climatology of Arctic Sea Ice Lead Orientation and Frequency from AMSR-E, Remote Sensing, 6, 1451–1475, https://doi.org/10.3390/rs6021451, https://www.mdpi.com/2072-4292/6/2/1451, 2014.

10 Coon, M., Kwok, R., Levy, G., Pruis, M., Schreyer, H., and Sulsky, D.: Arctic Ice Dynamics Joint Experiment (AIDJEX) assumptions revisited and found inadequate, Journal of Geophysical Research: Oceans, 112, C11S90, https://doi.org/10.1029/2005JC003393, http://onlinelibrary.wiley.com/doi/10.1029/2005JC003393/abstract, 2007.

Coon, M. D., Maykut, A., G., Pritchard, R. S., Rothrock, D. A., and Thorndike, A. S.: Modeling The Pack Ice as an Elastic-Plastic Material, AIDJEX BULLETIN, No. 24, 1–106, 1974.

15 Dansereau, V., Weiss, J., Saramito, P., and Lattes, P.: A Maxwell elasto-brittle rheology for sea ice modelling, The Cryosphere, 10, 1339–1359, https://doi.org/10.5194/tc-10-1339-2016, http://www.the-cryosphere.net/10/1339/2016/, 2016.

Dansereau, V., Démery, V., Berthier, E., Weiss, J., and Ponson, L.: Fault orientation in damage failure under compression, arXiv:1712.08530 [cond-mat, physics:physics], http://arxiv.org/abs/1712.08530, arXiv: 1712.08530, 2017.

Dethloff, K., Rex, M., and Shupe, M.: Multidisciplinary drifting Observatory for the Study of Arctic Climate (MOSAiC), EGU General

20 Assembly Conference Abstracts, 18, https://ui.adsabs.harvard.edu/#abs/2016EGUGA..18.3064D/abstract, 2016.

Dumont, D., Gratton, Y., and Arbetter, T. E.: Modeling the Dynamics of the North Water Polynya Ice Bridge, Journal of Physical Oceanography, 39, 1448–1461, https://doi.org/10.1175/2008JPO3965.1, https://journals.ametsoc.org/doi/abs/10.1175/2008JPO3965.1, 2009.

Erlingsson, B.: Two-dimensional deformation patterns in sea ice, Journal of Glaciology, 34, 301–308, 1988.

Flato, G. M. and Hibler, W. D.: Modeling Pack Ice as a Cavitating Fluid, Journal of Physical Oceanography, 22, 626–651,

25 https://doi.org/10.1175/1520-0485(1992)022<0626:MPIAAC>2.0.CO;2, https://journals.ametsoc.org/doi/abs/10.1175/1520-0485(1992)022%3C0626:MPIAAC%3E2.0.CO%3B2, 1992.

Girard, L., Weiss, J., Molines, J. M., Barnier, B., and Bouillon, S.: Evaluation of high-resolution sea ice models on the basis of statistical and scaling properties of Arctic sea ice drift and deformation, Journal of Geophysical Research: Oceans, 114, C08 015, https://doi.org/10.1029/2008JC005182, http://onlinelibrary.wiley.com/doi/10.1029/2008JC005182/abstract, 2009.

30 Girard, L., Bouillon, S., Weiss, J., Amitrano, D., Fichefet, T., and Legat, V.: A new modeling framework for sea-ice mechanics based on elasto-brittle rheology, Annals of Glaciology, 52, 123–132, https://doi.org/10.3189/172756411795931499, 2011.

Heorton, H. D. B. S., Feltham, D. L., and Tsamados, M.: Stress and deformation characteristics of sea ice in a high-resolution, anisotropic sea ice model, Phil. Trans. R. Soc. A, 376, 20170 349, https://doi.org/10.1098/rsta.2017.0349, http://rsta.royalsocietypublishing.org/content/376/2129/20170349, 2018.

35 Herman, A.: Discrete-Element bonded-particle Sea Ice model DESIgn, version 1.3a - model description and implementation, Geoscientific Model Development, 9, https://doi.org/10.5194/gmd-9-1219-2016, https://ui.adsabs.harvard.edu/#abs/2016GMD.....9.1219H/abstract, 2016.

Hibler, W. D.: A Dynamic Thermodynamic Sea Ice Model, Journal of Physical Oceanography, 9, 815–846, https://doi.org/10.1175/1520-0485(1979)009<0815:ADTSIM>2.0.CO;2, http://journals.ametsoc.org/doi/abs/10.1175/1520-0485%281979%29009%3C0815%3AADTSIM%3E2.0.CO%3B2, 1979.

Hibler, W. D. and Schulson, E. M.: On modeling the anisotropic failure and flow of flawed sea ice, Journal of Geophysical Research: Oceans, 105, 17 105–17 120, https://doi.org/10.1029/2000JC900045, http://onlinelibrary.wiley.com/doi/10.1029/2000JC900045/abstract, 2000.

Hunke, E. C.: Viscous–Plastic Sea Ice Dynamics with the EVP Model: Linearization Issues, Journal of Computational Physics, 170, 18–38, https://doi.org/10.1006/jcph.2001.6710, http://www.sciencedirect.com/science/article/pii/S0021999101967105, 2001.

Hunke, E. C. and Dukowicz, J. K.: An Elastic–Viscous–Plastic Model for Sea Ice Dynamics, Journal of Physical Oceanography, 27, 1849–1867, https://doi.org/10.1175/1520-0485(1997)027<1849:AEVPMF>2.0.CO;2, http://journals.ametsoc.org/doi/abs/10.1175/1520-0485(1997)027%3C1849:AEVPMF%3E2.0.CO;2, 1997.

Hutchings, J. K., Heil, P., and Hibler, W. D.: Modeling Linear Kinematic Features in Sea Ice, Monthly Weather Review, 133, 3481–3497, https://doi.org/10.1175/MWR3045.1, http://journals.ametsoc.org/doi/abs/10.1175/MWR3045.1, 2005.

Hutter, K. and Rajagopal, K. R.: On flows of granular materials, Continuum Mechanics and Thermodynamics, 6, 81–139, https://doi.org/10.1007/BF01140894, https://doi.org/10.1007/BF01140894, 1994.

Hutter, N., Martin, L., and Dimitris, M.: Scaling Properties of Arctic Sea Ice Deformation in a High-Resolution Viscous-Plastic Sea Ice Model and in Satellite Observations, Journal of Geophysical Research: Oceans, 123, 672–687, https://doi.org/10.1002/2017JC013119, https://agupubs.onlinelibrary.wiley.com/doi/abs/10.1002/2017JC013119, 2018a.

Hutter, N., Zampieri, L., and Losch, M.: Leads and ridges in Arctic sea ice from RGPS data and a new tracking algorithm, The Cryosphere Discussions, pp. 1–27, https://doi.org/https://doi.org/10.5194/tc-2018-207, https://www.the-cryosphere-discuss.net/tc-2018-207/, 2018b.

Ip, C. F., Hibler, W. D., and Flato, G. M.: On the effect of rheology on seasonal sea-ice simulations, Annals of Glaciology, 15, 17–25, 1991.

Kwok, R.: Deformation of the Arctic Ocean Sea Ice Cover between November 1996 and April 1997: A Qualitative Survey, in: IUTAM Symposium on Scaling Laws in Ice Mechanics and Ice Dynamics, edited by Dempsey, J. P. and Shen, H. H., no. 94 in Solid Mechanics and Its Applications, pp. 315–322, Springer Netherlands, https://doi.org/10.1007/978-94-015-9735-7_26, http://link.springer.com/chapter/10.1007/978-94-015-9735-7_26, 2001.

Lemieux, J.-F. and Tremblay, B.: Numerical convergence of viscous-plastic sea ice models, Journal of Geophysical Research: Oceans, 114, https://doi.org/10.1029/2008JC005017, https://agupubs.onlinelibrary.wiley.com/doi/abs/10.1029/2008JC005017, 2009.

Lindsay, R. W. and Rothrock, D. A.: Arctic sea ice leads from advanced very high resolution radiometer images, Journal of Geophysical Research: Oceans, 100, 4533–4544, https://doi.org/10.1029/94JC02393, https://agupubs.onlinelibrary.wiley.com/doi/abs/10.1029/94JC02393, 1995.

Losch, M., Menemenlis, D., Campin, J.-M., Heimbach, P., and Hill, C.: On the formulation of sea-ice models. Part 1: Effects of different solver implementations and parameterizations, Ocean Modelling, 33, 129–144, https://doi.org/10.1016/j.ocemod.2009.12.008, https://www.sciencedirect.com/science/article/pii/S1463500309002418, 2010.

Marko John R. and Thomson Richard E.: Rectilinear leads and internal motions in the ice pack of the western Arctic Ocean, Journal of Geophysical Research, 82, 979–987, https://doi.org/10.1029/JC082i006p00979, https://agupubs.onlinelibrary.wiley.com/doi/10.1029/JC082i006p00979, 1977.

Marshall, J., Adcroft, A., Hill, C., Perelman, L., and Heisey, C.: A finite-volume, incompressible Navier Stokes model for studies of the ocean on parallel computers, Journal of Geophysical Research: Oceans, 102, 5753–5766, https://doi.org/10.1029/96JC02775, http://onlinelibrary.wiley.com/doi/10.1029/96JC02775/abstract, 1997.

Miller, P. A., Laxon, S. W., and Feltham, D. L.: Improving the spatial distribution of modeled Arctic sea ice thickness, Geophysical Research Letters, 32, https://doi.org/10.1029/2005GL023622, https://agupubs.onlinelibrary.wiley.com/doi/abs/10.1029/2005GL023622, 2005.

Overland, J. E., McNutt, S. L., Salo, S., Groves, J., and Li, S.: Arctic sea ice as a granular plastic, Journal of geophysical research, 103, 21 845–21 868, https://www.researchgate.net/profile/James_Overland/publication/240487097_Arctic_sea_ice_as_a_granular_plastic/links/55cb6a2c08aeb975674c796b.pdf, 1998.

Popov, E. P.: Mechanics of Materials, Prentice Hall, Englewood Cliffs, N.J, 2 edition edn., 1976.

Pritchard, R. S.: Mathematical characteristics of sea ice dynamics models, Journal of Geophysical Research: Oceans, 93, 15 609–15 618, https://doi.org/10.1029/JC093iC12p15609, http://onlinelibrary.wiley.com/doi/10.1029/JC093iC12p15609/abstract, 1988.

Rampal, P., Bouillon, S., Ólason, E., and Morlighem, M.: neXtSIM: a new Lagrangian sea ice model, The Cryosphere, 10, 1055–1073, https://doi.org/10.5194/tc-10-1055-2016, http://www.the-cryosphere.net/10/1055/2016/, 2016.

Rothrock, D. A.: The steady drift of an incompressible Arctic ice cover, Journal of Geophysical Research, 80, 387–397, https://doi.org/10.1029/JC080i003p00387, http://onlinelibrary.wiley.com/doi/10.1029/JC080i003p00387/abstract, 1975.

Schmidt, G. A., Kelley, M., Nazarenko, L., Ruedy, R., Russell, G. L., Aleinov, I., Bauer, M., Bauer, S. E., Bhat, M. K., Bleck, R., Canuto, V., Chen, Y.-H., Cheng, Y., Clune, T. L., Genio, A. D., Fainchtein, R. d., Faluvegi, G., Hansen, J. E., Healy, R. J., Kiang, N. Y., Koch, D., Lacis, A. A., LeGrande, A. N., Lerner, J., Lo, K. K., Matthews, E. E., Menon, S., Miller, R. L., Oinas, V., Oloso, A. O., Perlwitz, J. P., Puma, M. J., Putman, W. M., Rind, D., Romanou, A., Sato, M., Shindell, D. T., Sun, S., Syed, R. A., Tausnev, N., Tsigaridis, K., Unger, N., Voulgarakis, A., Yao, M.-S., and Zhang, J.: Configuration and assessment of the GISS ModelE2 contributions to the CMIP5 archive, Journal of Advances in Modeling Earth Systems, 6, 141–184, https://doi.org/10.1002/2013MS000265, https://agupubs.onlinelibrary.wiley.com/doi/abs/10.1002/2013MS000265, 2014.

Schreyer, H. L., Sulsky, D. L., Munday, L. B., Coon, M. D., and Kwok, R.: Elastic-decohesive constitutive model for sea ice, Journal of Geophysical Research: Oceans, 111, C11S26, https://doi.org/10.1029/2005JC003334, http://onlinelibrary.wiley.com/doi/10.1029/2005JC003334/abstract, 2006.

Schulson, E. M.: Compressive shear faults within arctic sea ice: Fracture on scales large and small, Journal of Geophysical Research: Oceans, 109, C07 016, https://doi.org/10.1029/2003JC002108, http://onlinelibrary.wiley.com/doi/10.1029/2003JC002108/abstract, 2004.

Sirven, J. and Tremblay, B.: Analytical Study of an Isotropic Viscoplastic Sea Ice Model in Idealized Configurations, Journal of Physical Oceanography, 45, 331–354, https://doi.org/10.1175/JPO-D-13-0109.1, https://journals.ametsoc.org/doi/abs/10.1175/JPO-D-13-0109.1, 2014.

Spreen, G., Kwok, R., Menemenlis, D., and Nguyen, A. T.: Sea-ice deformation in a coupled ocean–sea-ice model and in satellite remote sensing data, The Cryosphere, 11, 1553–1573, https://doi.org/10.5194/tc-11-1553-2017, https://www.the-cryosphere.net/11/1553/2017/, 2017.

Stroeve, J., Barrett, A., Serreze, M., and Schweiger, A.: Using records from submarine, aircraft and satellites to evaluate climate model simulations of Arctic sea ice thickness, The Cryosphere, 8, 1839–1854, https://doi.org/10.5194/tc-8-1839-2014, http://www.the-cryosphere.net/8/1839/2014/, 2014.

Sulsky, D., Schreyer, H., Peterson, K., Kwok, R., and Coon, M.: Using the material-point method to model sea ice dynamics, Journal of Geophysical Research: Oceans, 112, C02S90, https://doi.org/10.1029/2005JC003329, http://onlinelibrary.wiley.com/doi/10.1029/2005JC003329/abstract, 2007.

Tremblay, L.-B. and Mysak, L. A.: Modeling Sea Ice as a Granular Material, Including the Dilatancy Effect, Journal of Physical Oceanography, 27, 2342–2360, https://doi.org/10.1175/1520-0485(1997)027<2342:MSIAAG>2.0.CO;2, http://journals.ametsoc.org/doi/abs/10.1175/1520-0485(1997)027%3C2342:MSIAAG%3E2.0.CO;2, 1997.

Tsamados, M., Feltham, D. L., and Wilchinsky, A. V.: Impact of a new anisotropic rheology on simulations of Arctic sea ice, Journal of Geophysical Research: Oceans, 118, 91–107, https://doi.org/10.1029/2012JC007990, http://onlinelibrary.wiley.com/doi/10.1029/2012JC007990/abstract, 2013.

Ungermann, M., Tremblay, L. B., Martin, T., and Losch, M.: Impact of the Ice Strength Formulation on the Performance of a Sea Ice Thickness Distribution Model in the Arctic, Journal of Geophysical Research: Oceans, pp. n/a–n/a, https://doi.org/10.1002/2016JC012128, http://onlinelibrary.wiley.com/doi/10.1002/2016JC012128/abstract, 2017.

Walter, B. A. and Overland, J. E.: The response of lead patterns in the Beaufort Sea to storm-scale wind forcing, Annals of Glaciology, 17, 219–226, https://doi.org/10.3189/S0260305500012878, https://www.cambridge.org/core/journals/annals-of-glaciology/article/div-classtitlethe-response-of-lead-patterns-in-the-beaufort-sea-to-storm-scale-wind-forcingdiv/43BF1A611FEAF0F5EA4DFFAA9236F11F, 1993.

Wang, K., Leppäranta, M., and Kõuts, T.: A study of sea ice dynamic events in a small bay, Cold Regions Science and Technology, 45, 83–94, https://doi.org/10.1016/j.coldregions.2006.02.002, http://www.sciencedirect.com/science/article/pii/S0165232X0600022X, 2006.

Wang, Q., Danilov, S., Jung, T., Kaleschke, L., and Wernecke, A.: Sea ice leads in the Arctic Ocean: Model assessment, interannual variability and trends, Geophysical Research Letters, 43, 7019–7027, https://doi.org/10.1002/2016GL068696, https://agupubs.onlinelibrary.wiley.com/doi/abs/10.1002/2016GL068696, 2016.

Weiss, J., Schulson, E. M., and Stern, H. L.: Sea ice rheology from in-situ, satellite and laboratory observations: Fracture and friction, Earth and Planetary Science Letters, 255, 1–8, https://doi.org/10.1016/j.epsl.2006.11.033, http://www.sciencedirect.com/science/article/pii/S0012821X06008430, 2007.

Wilchinsky, A. V. and Feltham, D. L.: Anisotropic model for granulated sea ice dynamics, Journal of the Mechanics and Physics of Solids, 54, 1147–1185, https://doi.org/10.1016/j.jmps.2005.12.006, http://www.sciencedirect.com/science/article/pii/S0022509606000032, 2006.

Wilchinsky, A. V., Feltham, D. L., and Hopkins, M. A.: Effect of shear rupture on aggregate scale formation in sea ice, Journal of Geophysical Research: Oceans, 115, C10 002, https://doi.org/10.1029/2009JC006043, http://onlinelibrary.wiley.com/doi/10.1029/2009JC006043/abstract, 2010.

Zhang, J. and Hibler, W. D.: On an efficient numerical method for modeling sea ice dynamics, Journal of Geophysical Research: Oceans, 102, 8691–8702, https://doi.org/10.1029/96JC03744, http://onlinelibrary.wiley.com/doi/10.1029/96JC03744/abstract, 1997.

Zhang, J. and Rothrock, D. A.: Effect of sea ice rheology in numerical investigations of climate, Journal of Geophysical Research: Oceans, 110, C08 014, https://doi.org/10.1029/2004JC002599, http://onlinelibrary.wiley.com/doi/10.1029/2004JC002599/abstract, 2005.